

An Efficient E-field Parallel Imaging Calibration Algorithm for Next-Generation Radio Telescopes

Adam P. Beardsley,¹★ Nithyanandan Thyagarajan,¹ Judd D. Bowman¹
and Miguel F. Morales²

¹Arizona State University, School of Earth and Space Exploration, Tempe, AZ 85287, USA

²University of Washington, Department of Physics, Seattle, WA 98195, USA

Accepted XXX. Received YYY; in original form ZZZ

ABSTRACT

Abstract here (250 words)

Key words: instrumentation: interferometers – techniques: image processing – techniques: interferometric

1 INTRODUCTION

In order to satisfy the survey speeds required for precision cosmology as well as searches for fast radio transients, radio astronomy is undergoing a paradigm shift toward interferometers consisting of hundreds to thousands of small, widefield antennas. Many arrays with this design are already built or under construction including the Hydrogen Epoch of Reionization Array¹ (HERA), the Murchison Widefield Array (MWA; Tingay et al. 2013; Bowman et al. 2013), the Precision Array for Probing the Epoch of Reionization (PAPER; Parsons et al. 2010), the LOw Frequency ARray (LOFAR; van Haarlem et al. 2013), the Canadian Hydrogen Intensity Mapping Experiment (CHIME; Bandura et al. 2014), the Long Wavelength Array (LWA; Ellingson et al. 2013), and the low frequency Square Kilometer Array (SKA1-Low Mellema et al. 2013).

Traditional radio correlators cross-multiply the voltage signals from all pairs of antennas, and the computation scales as the number of antennas squared, $O(N_a^2)$ (Bunton 2004). As the number of elements in future arrays grows, the computational cost will become prohibitively expensive, and exploring efficient correlator schemes is essential to enable next generation instruments (Lonsdale et al. 2000). Meanwhile, radio transient monitoring requires access to high time and frequency resolution data. For example, fast radio bursts (FRBs) are highly unexplored at low frequencies (< 1 GHz), but are expected to occur on timescales $\Delta t \sim 1\text{--}10$ ms (Thornton et al. 2013). Recording the full visibility matrix for $N_a \gtrsim 10^3$ arrays at this timescale leads to extremely high data write rates.

Direct imaging correlators are a new variety of radio correlator which aim to alleviate both the computational strain of forming N_a^2 correlations and the high data throughput associated with short timescale science. This is done by performing a spatial fast Fourier transform (FFT) to image the antenna voltages, then squaring and averaging in time. This process scales as $O(N_g \log_2 N_g)$, where

N_g is the number of grid points in the FFT (Morales 2011; Tegmark & Zaldarriaga 2009; Tegmark & Zaldarriaga 2010). For certain classes of telescopes, significantly those envisioned for next generation cosmology experiments, this scaling is a large improvement over the N_a^2 scaling of traditional methods. Furthermore, because images are generated online, the native output bandwidth will be lowered (assuming $N_g < N_a^2$), and has the potential to be lowered even further with online transient processing.

A handful of prototype direct imaging correlators have been tested on arrays including the Basic Element for SKA Training II (BEST-2) array (Foster et al. 2014), the Omniscope (Zheng et al. 2014), and an earlier pulsar timing experiment at GHz frequencies (Otoabe et al. 1994; Daishido et al. 2000). Each of these are examples of so-called FFT correlators – a subclass of direct imaging correlators which rely on identical antennas with restricted placement, which allows the FFT to be performed without gridding. We recently released the E-field Parallel Imaging Correlator (EPIC; Thyagarajan et al. 2015), which is a software implementation of the Modular Optimal Frequency Fourier (MOFF; Morales 2011) imaging algorithm. This architecture leverages the software holography/A-transpose framework to grid electric field data streams before performing the spatial FFT, allowing for an optimal map without placing constraints on array layout or requiring identical antennas (Morales & Matejek 2009; Bhatnagar, S. et al. 2008; Tegmark 1997).

A challenge common to all direct imaging algorithms is calibration of the antenna gains. Traditionally, pair-wise visibilities are written to disk and used to calibrate offline. However, a direct imaging correlator mixes the signals from all antennas before averaging and writing to disk, making calibration a requirement at the front end. Previous solutions have involved applying calibration solutions generated from a parallel FX correlator (Zheng et al. 2014; Foster et al. 2014), or integrating a dedicated FX correlator which periodically formed the full visibility matrix to solve for gains (Wijnholds & van der Veen 2009; de Vos et al. 2009). While these solutions were sufficient to enable the exploration of FFT correlators and beamformers, they will not scale to future arrays with $N_a \gtrsim 10^3$.

★ E-mail: Adam.Beardsley@asu.edu

¹ <http://reionization.org>

Here we present the E-field Parallel Imaging Calibration (EPI-Cal) algorithm – a novel solution to the calibration problem, which can be integrated into direct imaging correlators and scales only as the number of antennas, $O(N_a)$. This method uses a correlation of the uncalibrated antenna signal stream with an output image pixel from the backend of the correlator to solve for the complex gains of the antennas. Because the calibration must be applied before gridding and imaging, our solution requires an iterative approach where the data from one time series is used to update the gains which are applied to the following time series. An example implementation of the algorithm is available with the EPIC software package².

We establish the mathematical framework and derive the calibration algorithm in §2. We then demonstrate the algorithm in simulations in §3, and apply to a sample LWA data set in §4. Then we discuss the noise properties of the resulting gain solutions in §5. Finally we conclude and discuss potential extensions to the algorithm in §6.

2 MATHEMATICAL FRAMEWORK

We begin by establishing the mathematical framework for the calibration problem. We derive the calibration solutions for the MOFF algorithm (adopting the notation of Thyagarajan et al. 2015), but note the result is easily extended to FFT correlator algorithms by removing the gridding step.

The electric field incident on the ground, $\tilde{E}(\mathbf{r}, f, t)$, is related to the sky electric field, $E(\hat{\mathbf{s}}, f, t)$, through a Fourier transform.

$$\tilde{E}(\mathbf{r}, f, t) = \int E(\hat{\mathbf{s}}, f, t) e^{-2\pi i \mathbf{r} \cdot \hat{\mathbf{s}}} d^2 \hat{\mathbf{s}} \quad (1)$$

Here $\hat{\mathbf{s}}$ denotes the sine-projected unit vector for the sky angle, \mathbf{r} is the observer’s location (measured in wavelengths relative to an arbitrary origin), and f and t denote the frequency and time dependence, respectively. We will encounter several quantities which we attempt to estimate. We distinguish the “true” values with a superscript T , while the estimates are denoted with a prime. We define the true antenna signal as a convolution of the antenna voltage pattern, \tilde{W} , with the electric field on the ground.

$$\tilde{E}_a^T(f, t) \equiv \int \tilde{W}_a(\mathbf{r} - \mathbf{r}_a) \tilde{E}(\mathbf{r}, f, t) d^2 \mathbf{r} \quad (2)$$

The subscript a labels the antenna, and \mathbf{r}_a is the location of antenna a .

We next model the measured, uncalibrated electric field as a multiplicative complex gain and an additive noise term applied to the true antenna electric field.

$$\tilde{E}_a(f, t) = g_a^T(f, t) \tilde{E}_a^T(f, t) + \tilde{n}_a(f, t) \quad (3)$$

Note that this quantity is neither a true or estimated value. The noise term is strictly receiver noise – noise introduced by the instrument. Any sky noise is implicitly included in the time dependence of the sky electric field. As the noise of modern low frequency arrays is heavily dominated by sky noise, we will neglect \tilde{n}_a for now, but will inspect its effects at the end of this section.

The goal of our calibration algorithm will be to estimate the antenna gains. We will assume the gains have no time dependence within the timescale of finding our solutions. *cite someone about gain stability*. Furthermore, we will treat each frequency channel independently, and drop the f to simplify notation.

The MOFF algorithm next calls for a calibration. We will assume we have formed an estimate of the gains after n iterations of a calibration loop, and derive an updated $n + 1$ estimate. Typically calibration amounts to dividing the measured fields by the gain (in the case of sky noise dominance), or multiplying by the complex conjugate of the gain (receiver noise dominance). We will abstain from this choice for now, and instead use a multiplicative factor $h_a^{(n)}$ to represent the application of our n^{th} -loop estimate of the gain for antenna a :

$$\tilde{E}'_a = h_a^{(n)} \tilde{E}_a \quad (4)$$

where,

$$h_a^{(n)} = \begin{cases} 1/g_a^{(n)} & \text{sky noise dominated} \\ g_a^{*(n)} & \text{receiver noise dominated.} \end{cases} \quad (5)$$

A dirty image is next formed by gridding the calibrated fields with the antenna voltage pattern, Fourier transforming, squaring, and averaging in time. The estimated value for a pixel, $\hat{\mathbf{s}}_i$, can be expressed as

$$I'(\hat{\mathbf{s}}_i) = \left\langle \left| \frac{1}{N_a} \sum_i e^{2\pi i \mathbf{r}_i \cdot \hat{\mathbf{s}}_i} \sum_a \tilde{W}_a(\mathbf{r}_i - \mathbf{r}_a) h_a^{(n)} g_a^T \tilde{E}_a^T(t) \right|^2 \right\rangle_t \quad (6)$$

This is the final output of the MOFF correlator. However, for calibration purposes we will be interested in the electric field image just prior to squaring and averaging.

$$E'(\hat{\mathbf{s}}_i, t) = \frac{1}{N_a} \sum_i e^{2\pi i \mathbf{r}_i \cdot \hat{\mathbf{s}}_i} \sum_a \tilde{W}_a(\mathbf{r}_i - \mathbf{r}_a) h_a^{(n)} g_a^T \tilde{E}_a^T(t) \quad (7)$$

We can simplify this expression by exchanging the sums to transform the beam term into sky coordinates.

$$\begin{aligned} E'(\hat{\mathbf{s}}_i, t) &= \frac{1}{N_a} \sum_a h_a^{(n)} g_a^T \tilde{E}_a^T(t) e^{2\pi i \hat{\mathbf{s}}_i \cdot \mathbf{r}_a} \sum_i \tilde{W}_b(\mathbf{r}_i - \mathbf{r}_a) e^{2\pi i \hat{\mathbf{s}}_i \cdot (\mathbf{r}_i - \mathbf{r}_a)} \\ &= \frac{1}{N_a} \sum_a h_a^{(n)} g_a^T \tilde{E}_a^T(t) e^{2\pi i \hat{\mathbf{s}}_i \cdot \mathbf{r}_a} W_a(\hat{\mathbf{s}}_i) \end{aligned} \quad (8)$$

Next we move toward the feedback calibration outlined in Morales 2011. The calibration loop described there assumed a simple sky of a single point source, but we aim for a more generalized solution for arbitrarily complex sky models. As such the quantity we wish to inspect is a correlation of the uncalibrated antenna signals input to the correlator with the holographic electric field image output from the correlator. We define the quantity,

$$C_{a, \hat{\mathbf{s}}_0}^{(n)} \equiv \langle \tilde{E}_a(t) E'^*(\hat{\mathbf{s}}_0, t) \rangle_t, \quad (9)$$

where the superscript n again represents the quantity formed in the n^{th} calibration loop, and $\hat{\mathbf{s}}_0$ is the pixel center nearest a bright calibrator of interest. The following will hold for any chosen pixel, $\hat{\mathbf{s}}_0$, though it is advantageous to choose a pixel which contains a bright source to achieve a high signal to noise.

Plugging equation 8 into equation 9, we find,

$$\begin{aligned} C_{a, \hat{\mathbf{s}}_0}^{(n)} &= \left\langle g_a^T \tilde{E}_a^T(t) \frac{1}{N_a} \sum_b h_b^{*(n)} g_b^T \tilde{E}_b^*(t) e^{-2\pi i \hat{\mathbf{s}}_0 \cdot \mathbf{r}_b} W_b^*(\hat{\mathbf{s}}_0) \right\rangle_t \\ &= \frac{g_a^T}{N_a} \sum_b h_b^{*(n)} g_b^T W_b^*(\hat{\mathbf{s}}_0) e^{-2\pi i \hat{\mathbf{s}}_0 \cdot \mathbf{r}_b} \langle \tilde{E}_a^T \tilde{E}_b^* \rangle_t \\ &= \frac{g_a^T}{N_a} \sum_b h_b^{*(n)} g_b^T W_b^*(\hat{\mathbf{s}}_0) e^{-2\pi i \hat{\mathbf{s}}_0 \cdot \mathbf{r}_b} \tilde{V}_{ab}^T \end{aligned} \quad (10)$$

where in the second step we group time-dependent terms, and in

² <http://github.com/nithyanandan/EPIC>

the third we define the true visibilities as the correlation between true antenna electric field measurements. It is easy to see from here that the net effect of including the receiver noise term, $\tilde{n}_a(f, t)$, will result in added noise on the true visibilities. In principle this can include any noise correlations between antennas. The implementation included in the EPIC software package restricts the noise term to include only the auto-correlation noise bias, and assumes baseline dependent noise is zero mean.

Finally, we find an update to our gain solution by assuming our current estimate of the gains, $g_b^{(n)}$, is approximately correct and substitute into the sum for the true gains. We also require model visibilities formed from sky and primary beam models in place of true visibilities.

$$g_a^{(n+1)} = C_{a, \hat{s}_0}^{(n)} N_a \left[\sum_b h_b^{*(n)} g_b^{*(n)} W_b^*(\hat{s}_0) e^{-2\pi i \hat{s}_0 \cdot \mathbf{r}_b} \tilde{V}_{ab}^T \right]^{-1} \quad (11)$$

This equation is our prescription for estimating the antenna gains of a direct imaging array. The approach is iterative in nature, and requires a sky model. However, the sky model can be precomputed offline, and the online computation complexity scales only as $\mathcal{O}(N_a)$ as we form a $C_{a, \hat{s}_0}^{(n)}$ for each antenna. In the case where $h_b = 1/g_b$ (typical calibration procedure for sky-noise dominated systems), this simplifies slightly.

$$g_a^{(n+1)} = C_{a, \hat{s}_0}^{(n)} N_a \left[\sum_b W_b^*(\hat{s}_0) e^{-2\pi i \hat{s}_0 \cdot \mathbf{r}_b} \tilde{V}_{ab}^T \right]^{-1} \quad (12)$$

While testing we found equation 11 resulted in oscillatory gain solutions as it was iterated, as is often the case in iterative minimization methods. To mitigate this we introduce a damping factor, $0 \leq \gamma < 1$, which is used to attenuate the gain update, effectively giving the solutions memory of previous iterations.

$$g_a^{(n+1)} = (1 - \gamma) g_a^{(n+1)} + \gamma g_a^{(n)} \quad (13)$$

We found that while equation 11 does indeed converge on good solutions, the process is faster by tuning the damping factor. We note the small difference between $g_a^{(n+1)}$ and $g_a'^{(n+1)}$, where the prime indicates our current best estimate of the true gain, while no prime is actually used in the iterative calibration loop. Once the loop converges the difference is a longer effective integration for the non-primed version (lower thermal noise).

We show schematically the process of calibrating a direct imaging correlator in figure 1. Computationally expensive steps that must be performed “on-chip” are shown inside the gray box. The uncalibrated antenna signals are tapped out after the F-engine and correlated against the output image pixel of interest. The correlated values are then passed off-chip to estimate the gains using equation 11, and additional fitting if desired. The gains are then passed back to the correlator to update the calibration for subsequent data streams.

An important feature to note is that, like the MOFF-generated images themselves, equations 11 and 12 include the antenna auto-correlations (the sum is over *all* b , not excluding a). It can be difficult to perfectly model the noise bias from auto-correlations, which can often times be far brighter than the visibilities themselves. It can therefore be beneficial to subtract this term directly from $C_{a, \hat{s}_0}^{(n)}$, and exclude the $b = a$ term in the sum.

$$C_{a, \hat{s}_0}^{(n)} \rightarrow C_{a, \hat{s}_0}^{(n)} - \frac{1}{N_a} h_a^{*(n)} W_a^* e^{-2\pi i \hat{s}_0 \cdot \mathbf{r}_a} \langle |\tilde{E}_a|^2 \rangle_t \quad (14)$$

This requires generating these correlations, which again only scale as $\mathcal{O}(N_a)$, and are generally useful for array diagnostics.

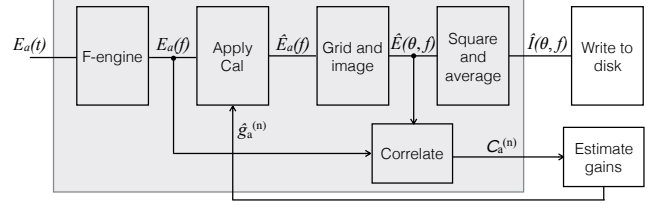


Figure 1. The general data flow of the MOFF correlator, with a feedback calibration loop. A pixel from the (unsquared) image is tapped out and correlated against the input antenna electric field signals to form $C_{a, \hat{s}_0}^{(n)}$ coefficients, which are used to estimate the antenna gains. These gain estimates are then fed back into the correlator to be applied to subsequent data, and the process is repeated. The gray box shows operations which must be done at high speed (before averaging in time), which white boxes show operations which can be performed “off-chip”.

We conclude this section by connecting our calibration expression to that found in a visibility framework. In the limit of a single bright calibrating source at phase center, we can greatly simplify equations 10 and 11. We will assume the beams are normalized such that $W(0) = 1$. We can further drop the exponential phase terms because $\hat{s}_0 = 0$. We then absorb the true gains and gain corrections into the true visibilities in equation 10 to express as a sum of measured visibilities.

$$C_{a, 0}^{(n)} \rightarrow \frac{1}{N_a} \sum_b h_b^{*(n)} \tilde{V}_{ab} \quad (15)$$

We next plug this expression into equation 11 to find our simplified calibration solution for a single bright point source. Because our sky is a single bright point source, the model visibilities are simply the flux of the source, S_{src} .

$$g_a^{(n+1)} \rightarrow \left[\sum_b h_b^{*(n)} \tilde{V}_{ab} \right] \times \left[S_{\text{src}} \sum_b h_b^{*(n)} g_b^{*(n)} \right]^{-1} \quad (16)$$

This is simply a gain-weighted sum of the measured visibilities over the flux of the source, which is indeed the limiting result from a visibility approach, for example seen in Mitchell et al. 2008. The ability to recover the equivalent expression despite not actually forming the visibilities is a result of the fact that only sums over visibilities come into the FX solution, as was described in Morales 2011. We have confirmed the limiting case equivalence here, and will explore the more general case in more detail in § 5.

3 SIMULATION

We first demonstrate our calibration method through a controlled simulation. A complex gain is created for each antenna with random phase and amplitude, which is used to corrupt the simulated data stream, then we attempt to recover the gains using our calibration routine. The simulation software used is included in the EPIC package.

Our simulated signal consists of 10 random point sources with flux densities $0.5 \text{ Jy} \lesssim S \lesssim 1 \text{ Jy}$. For an antenna array we use the inner 51 antennas of the MWA layout (Beardsley et al. 2012), within a bounding box of 150 m. The antenna voltage pattern used is a 4.4 m square tophat on the ground. Because our algorithm treats frequency channels independently, we simulate only one channel.

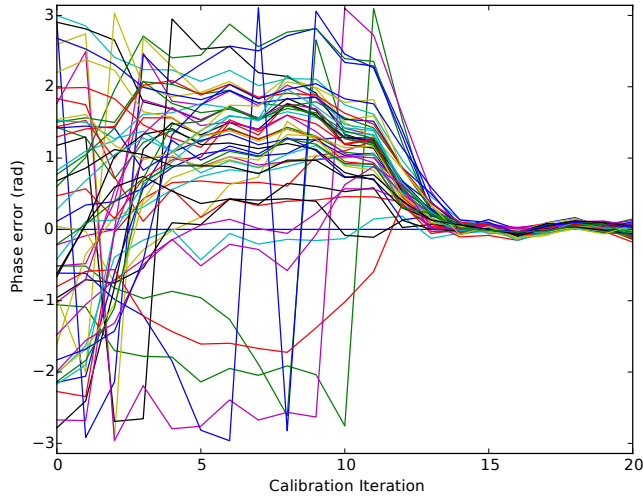


Figure 2. Phase error of gain estimates as a function of iteration for simulated calibration. The gains were initialized with random phases, but the calibration loop was able to recover the correct phases after about 15 iterations. Each line represents an antenna in our 51 MWA antenna sample.

For context we treat this channel as a single 40 kHz, meaning each subsequent timestep is separated by 25 μ s.

For our unknown gains, we create a set of random numbers with amplitude 1 ± 0.25 , and completely random phase. These are our “true gains”, and we apply them to the frequency-domain simulated antenna electric fields as in equation 3. Our analysis is blind to these values until the end of the process to check accuracy. The gain estimates are initialized with unity, $g_a^{(0)} = 1$.

We next process and image 400 time steps (10 ms). We also form the correlations, $C_{a,\hat{s}_0}^{(0)}$, used in our calibration loop. The pixel used for the correlation is the source with the largest apparent flux (intrinsic flux attenuated by the primary beam). These correlation values are used to update the gain estimates, which in turn are used to calibrate the following 400 time steps. Through experimentation we found a damping factor of $\gamma = 0.35$ resulted in the quickest convergence in this simulation.

The calibration loop continues by updating the gain estimates every 400 time steps. The phases of our gain estimates are shown in figure 2 for 20 such iterations. The phase error plotted is the phase relative to the true gain for each antenna (various colored lines). One antenna was used as a reference to fix the absolute phase, so has zero phase error. The other 50 antennas are shown to have error spanning 2π initially, and after about 10 iterations lock into a solution, settling down to noise levels around iteration 15 (0.15 s). We stop the simulation when the updated gains trace the thermal noise of the simulated sources, which can be seen by the coherence of the 50 antenna gains after iteration 15.

The estimated gain amplitudes for the simulations are shown in figure 3. The quantity plotted is the magnitude of the estimated gains over the true gains, $|g_a^{(n)} / g_a^T|$, which places all antennas on the same scale. We can see the amplitudes converge toward their true values around the same time as the phases (iteration ~ 15). At the beginning of calibration we can see the value of the damping factor. At $n = 0$, a couple of gains are shown to have abnormally high amplitude estimates, notably one about 3.3 times its true value (red line). These unbalanced high estimates caused the entire set of gains to be under estimated at $n = 1$, even with a damping factor of 0.35.

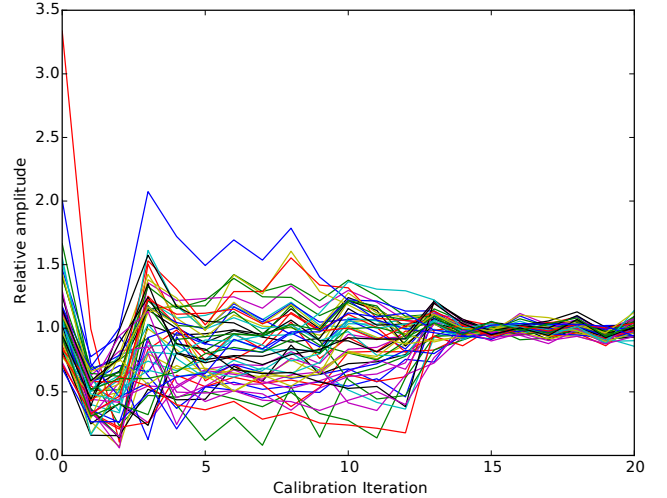


Figure 3. Gain estimate amplitudes as a function of iteration for simulated calibration. Again, each line represents an antenna in the 51 MWA antenna sample. The gain estimates were initialized randomly, while the true values were unity. After about 15 iterations we see the calibration loop has settled around the correct values, with only noise remaining.

By $n = 5$ the unbalanced amplitudes have been damped out and the calibration continues. Without the damping factor, the oscillation seen in the first couple iterations would have been significantly larger and taken much longer to fade out.

Images created at the beginning of calibration and at the end are shown in figure 4. Each image is 10 ms integration, corresponding to all snapshot images created with a given set of gain estimates. The top panel shows the image produced with our initialized unity gains. Because the phases are completely random, the image is essentially noise with the primary beam evident. After 20 iterations, the image is far more clear, shown in the bottom panel. Each of the ten simulated sources are clearly visible, indicated with red circles.

4 APPLICATION TO LWA DATA

We next demonstrate our calibration algorithm using an observation from the LWA station in New Mexico. The data is from the LWA narrow-band transient buffer (TBN), with time ordered voltage data from 255 antennas within a core radius of 100 m. The central frequency is 74.03 MHz, and a bandwidth of 100 kHz and writeout timescale of 5.12 ms (frequency channel resolution of 195.3125 Hz). For this demonstration we limit ourselves to a single polarization.

After correcting for geometric cable delays, the instrument is naturally well calibrated, as was seen in the demonstration of the EPIC imager in Thyagarajan et al. 2015. However, we will aim to improve yet on this calibration using our algorithm.

We proceed by forming model visibilities. We model only two bright objects as point sources: Cyg A with flux 16611.68 Jy (Cohen et al. 2007); and Cas A with flux 17693.9 Jy (Kassim et al. 2007). Because the raw data is attenuated by the primary beam of the instrument, we also account for this in our model using beam values consistent with Hicks et al. (2012).

We made several choices while studying the behavior of the LWA data to improve our calibration. We inspected the amplitudes of the voltages to be roughly consistent with average gain amplitudes of 0.25, so we initialized our gains at this level to allow the

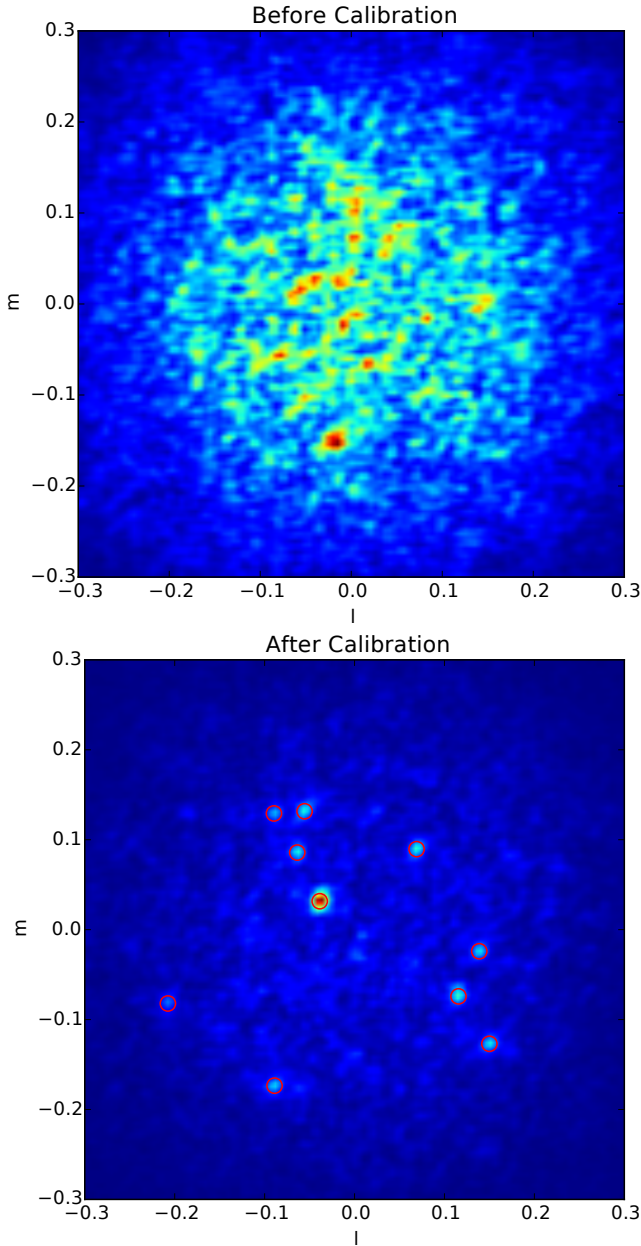


Figure 4. Images formed during simulated calibration. *Top:* An image generated from a single frequency channel and 10 ms integration after the gain estimates are randomized. As expected with random phases, the image is completely noisy, with the shape of the primary beam evident. *Bottom:* An image formed after calibration, again with a single frequency channel and 10 ms integration. The ten simulated (and modeled) point sources are easily visible, and highlighted with red circles.

calibration to converge quickly. We also found a boost in signal to noise is achieved easily by averaging frequency channels and assuming the gains are constant within a sub-band. Here we average solutions across 150 channels, or about 29 kHz. With a fractional bandwidth $B/f_0 = 3.9 \times 10^{-4}$, we felt safe assuming a smooth bandpass. Because there is still a fair amount of noise in the data, a damping factor of $\gamma = 0.7$ was adopted.

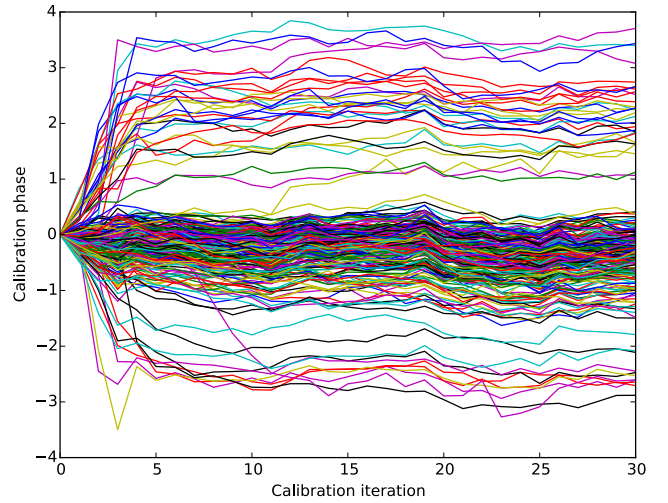


Figure 5. Gain phase solutions as a function of calibration iteration for an LWA TBN observation. The gain estimates are initialized with zero phase, but quickly span a 2π range, and settle into relatively flat, albeit noisy, solutions. The majority of phases congregate near zero, which is not surprising given the fairly good quality image produced from uncalibrated data.

Finally, we found that seven antennas³ produced unstable gain solutions, and in fact corrupted the ensemble. We therefore flagged these antennas for our analysis, resulting in a total of 248 antennas to calibrate. In each calibration loop, we form our feedback correlations and update our gain estimates over 10 timestamps (51.2 ms). We iterate the loop 30 times for a total of 1.536 seconds. The results of this experiment are shown in figures 5 – 7.

Figure 5 shows the phase of our gain estimates over our 30 calibration iterations, again with each colored line representing a different antenna. Given the quality of uncalibrated image demonstrated in Thyagarajan et al. (2015), it is a bit surprising to see the phase variation in our solutions. However, the phases are relatively flat after about 15 iterations (modulo noise), and exhibit a central “trunk” where the majority of phases are congregated. This behavior is suggestive that while the uncalibrated voltages were able to produce a viable image, the minor changes from our solutions will focus the image and improve the quality. The actual location of the “trunk” (slightly negative) is simply determined by the reference antenna chosen to have identically zero phase, but happens to be slightly more positive than the bulk of antennas. We also note that some phases appear to exceed $\pm\pi$ radians, this is due to the unwrapping done for plotting clarity.

The gain amplitudes as a function of calibration iteration are shown in figure 6. There is a fairly wide range in gain amplitudes (from 0.12 to 0.59). However, this is not surprising due to the non-uniformity in the cables from the antennas to the receivers. Again, the amplitudes are noisy by relatively flat.

Figure 7 shows the improvement in the images due to our calibration. The left panel shows the uncalibrated image integrated over 51.2 ms, 29 kHz. Cyg A is prominent near the center of the image, and Cas A is also clearly visible in the upper right. The middle panel shows the image produced after calibration with identical integration time and bandwidth. The sidelobes throughout the image

³ LWA antenna IDs 48, 85, 124, 148, 203, 217, and 244 were flagged.

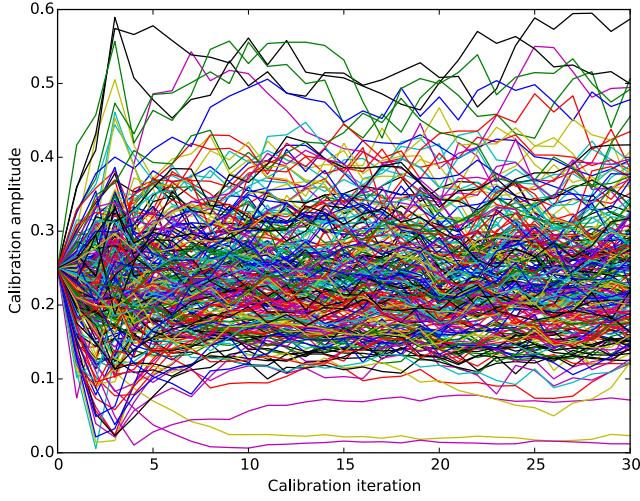


Figure 6. Gain amplitudes as a function of calibration iteration for an LWA TBN observation. The gains estimates were initialized with amplitude 0.25 after inspection of the electric field values compared to our model sky. The solutions are noisy, but flat. The range in amplitudes is due to the non-uniformity of cables between the LWA antennas and receivers.

are significantly suppressed, and the galactic plane is much more evident. We also note that the feature just to the right of Cyg A is dimmer in the calibrated image, better matching the expected flux from the global sky model (GSM, [de Oliveira-Costa et al. 2008](#)). We show the GSM modulated by two factors of the LWA primary beam in the right panel of figure 7 for reference.

To compare the image qualities quantitatively we compute the dynamic range, defined as the peak of the image over the noise level. We estimate the noise level as the median of the absolute deviation of the image. With this metric we find the calibrated image to have a 55% dynamic range improvement over the uncalibrated image.

5 NOISE ANALYSIS

Here we study the properties of our calibration solutions with respect to noise in the system. In order to compare to solutions from visibility-based calibration, we first derive the theoretical lower bound of the error in these solutions, given a set of measured visibilities, \mathbf{V} . We will do this through the Fisher information formalism and employ the Cramér-Rao lower bound

Assume we did form visibilities with some integration time. Assuming the noise on each visibility, σ_{ab} , is independent, we can write the likelihood function of measuring V_{ab} given the true value, the gains, and the noise.

$$\mathcal{L}(V_{ab}; \mathbf{g}) = \frac{1}{2\pi\sigma_{ab}^2} \exp \left[-\frac{|V_{ab} - g_a g_b^* V_{ab}^T|^2}{2\sigma_{ab}^2} \right] \quad (17)$$

Then the likelihood of the set of all visibilities is the product of all individual likelihoods.

$$\mathcal{L}(\mathbf{V}; \mathbf{g}) = \prod_a \prod_{b>a} \mathcal{L}(V_{ab}; \mathbf{g}) \quad (18)$$

The Fischer information matrix for the set of gain parameters is

$$\mathbf{F}_{ij}^g = \left\langle \frac{\partial \ln \mathcal{L}(\mathbf{V}; \mathbf{g})}{\partial g_i} \frac{\partial \ln \mathcal{L}(\mathbf{V}; \mathbf{g})}{\partial g_j} \right\rangle, \quad (19)$$

where the expectation is taken over all possible visibility measurements. We next evaluate the derivate of the log-likelihood.

$$\frac{\partial \ln \mathcal{L}(\mathbf{V}; \mathbf{g})}{\partial g_i} = \sum_{a \neq i} \frac{g_a^* V_{ai}^{T*} (V_{ai} - g_a g_i^* V_{ai}^T)}{2\sigma_{ai}^2} \quad (20)$$

In order to find the Cramér-Rao lower bound on the variance of the complex parameter, g_i , we consider the term of the Fischer matrix where the first derivative is taken with respect to g_i , and the second with g_i^* . The result is

$$\begin{aligned} \mathbf{F}_{ii}^g &= \left\langle \left[\sum_{a \neq i} \frac{g_a^* V_{ai}^{T*} (V_{ai} - g_a g_i^* V_{ai}^T)}{2\sigma_{ai}^2} \right] \times \right. \\ &\quad \left. \left[\sum_{b \neq i} \frac{g_b V_{bi}^T (V_{bi}^* - g_b^* g_i V_{bi}^{T*})}{2\sigma_{bi}^2} \right] \right\rangle \\ &= \sum_{a \neq i} \sum_{b \neq i} \frac{g_a^* g_b V_{ai}^{T*} V_{bi}^T}{4\sigma_{ai}^2 \sigma_{bi}^2} \langle V_{ai} V_{bi}^* - g_i g_b^* V_{ai} V_{bi}^{T*} \\ &\quad - g_a g_i^* V_{ai}^T V_{bi}^* + g_a g_b^* |g_i|^2 V_{ai}^T V_{bi}^{T*} \rangle \end{aligned} \quad (21)$$

The expected values are easy to evaluate. Each visibility will average to the “true” value times the respective gains. The term with two visibilities will include a noise bias on autocorrelation terms.

$$\langle V_{ai} V_{bi}^* \rangle = |g_i|^2 g_a g_b^* V_{ai} V_{bi}^{T*} + \sigma_{ai}^2 \delta_{ab} \quad (22)$$

Here δ_{ab} is the Kronecker delta selecting the term where $a = b$ and the noise correlates. Plugging in the expectation values, equation 21 simplifies greatly to

$$\mathbf{F}_{ii}^g = \sum_{a \neq i} \frac{|g_a V_{ia}^T|^2}{4\sigma_{ai}^2} \quad (23)$$

Finally we relate our result to the theoretical best uncertainty we can place on our unknown gain parameter using the Cramér-Rao lower bound.

$$\sigma_{gi}^2 \geq [\mathbf{F}_{ii}^g]^{-1} = \left[\sum_{a \neq i} \frac{|g_a V_{ia}^T|^2}{4\sigma_{ai}^2} \right]^{-1} \quad (24)$$

We next run a set of EPICal simulations to compare the noisy results to the theoretical lower bound given a set of equivalent visibilities. Each simulation is run with a simple sky of a single point source with flux 1 Jy. We add noise to the system by adding a Gaussian-random complex value to each channelized electric field antenna measurement as in equation 3. The “true” gains in our simulation are unity, as well as our initial estimate. This emulates a system where the initially volatile gain correction has been suppressed and only noise remains to corrupt our estimation, allowing us to run many simulations on a shorter timescale.

We vary two parameters in our simulations: the amount of noise added to our measurements, and the length of integration in each calibration loop.

6 DISCUSSION

ACKNOWLEDGEMENTS

This work has been supported by the National Science Foundation through award AST-1206552.

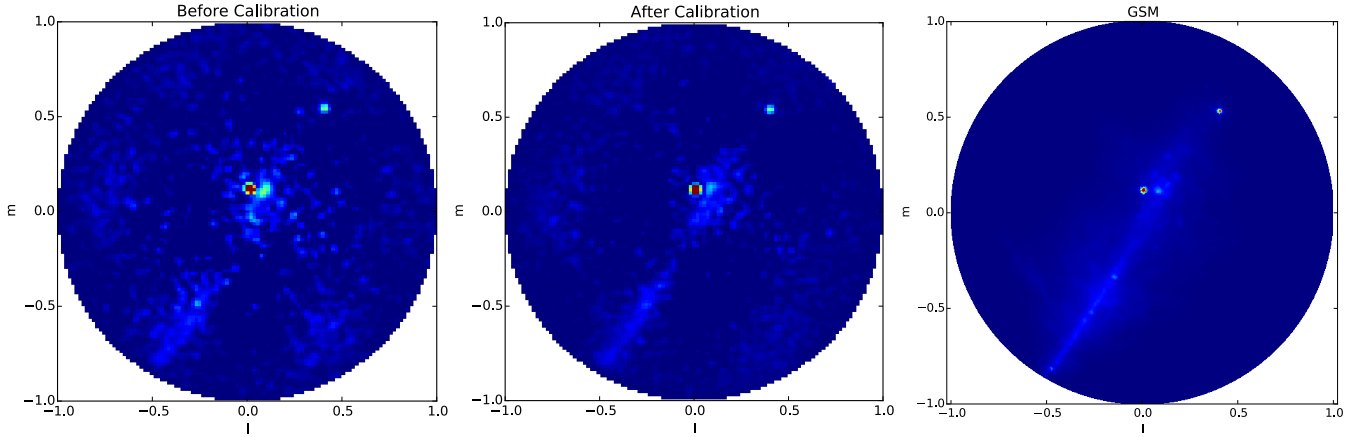


Figure 7. Images produced before (left) and after (middle) calibrating LWA data. These images were produced with 29 kHz bandwidth and 51.2 ms integration. The calibrated image shows significant reduction in sidelobe rumble throughout, while retaining the prominent Cyg A and Cas A sources. The galactic plane is also substantially more evident after calibration. For reference, the GSM is shown in the same coordinates and weighted by two factors of the LWA primary beam in the right panel.

REFERENCES

- Bandura K., et al., 2014, in Society of Photo-Optical Instrumentation Engineers (SPIE) Conference Series. p. 22 ([arXiv:1406.2288](#)), [doi:10.1117/12.2054950](#)
- Beardsley A. P., et al., 2012, *MNRAS*, **425**, 1781
- Bhatnagar, S. Cornwell, T. J. Golap, K. Uson, J. M. 2008, *A&A*, **487**, 419
- Bowman J. D., et al., 2013, *Publ. Astron. Soc. Australia*, **30**, 31
- Bunton J. D., 2004, *Experimental Astronomy*, **17**, 251
- Cohen A. S., Lane W. M., Cotton W. D., Kassim N. E., Lazio T. J. W., Perley R. A., Condon J. J., Erickson W. C., 2007, *AJ*, **134**, 1245
- Daishido T., et al., 2000, *Proc. SPIE*, 4015, 73
- Ellingson S. W., et al., 2013, *IEEE Transactions on Antennas and Propagation*, **61**, 2540
- Foster G., Hickish J., Magro A., Price D., Zarb Adami K., 2014, *Monthly Notices of the Royal Astronomical Society*, **439**, 3180
- Hicks B. C., et al., 2012, *Publications of the Astronomical Society of the Pacific*, **124**, pp. 1090
- Kassim N. E., et al., 2007, *ApJS*, **172**, 686
- Lonsdale C. J., Doeleman S. S., Cappallo R. J., Hewitt J. N., Whitney A. R., 2000, in Butcher H. R., ed., Society of Photo-Optical Instrumentation Engineers (SPIE) Conference Series Vol. 4015, Radio Telescopes. pp 126–134
- Mellema G., et al., 2013, *Experimental Astronomy*, **36**, 235
- Mitchell D., Greenhill L., Wayth R., Sault R., Lonsdale C., Cappallo R., Morales M., Ord S., 2008, *Selected Topics in Signal Processing, IEEE Journal of*, **2**, 707
- Morales M. F., 2011, *PASP*, **123**, 1265
- Morales M. F., Matejek M., 2009, *MNRAS*, **400**, 1814
- Otobe E., et al., 1994, *PASJ*, **46**, 503
- Parsons A. R., et al., 2010, *The Astronomical Journal*, **139**, 1468
- Tegmark M., 1997, *ApJ*, **480**, L87
- Tegmark M., Zaldarriaga M., 2009, *Phys. Rev. D*, **79**, 083530
- Tegmark M., Zaldarriaga M., 2010, *Phys. Rev. D*, **82**, 103501
- Thornton D., et al., 2013, *Science*, **341**, 53
- Thyagarajan N., Beardsley A. P., Bowman J. D., Morales M. F., 2015, [arXiv:1510.08318](#)
- Tingay S. J., et al., 2013, *PASA - Publications of the Astronomical Society of Australia*, **30**
- Wijnholds S., van der Veen A.-J., 2009, *Signal Processing, IEEE Transactions on*, **57**, 3512
- Zheng H., et al., 2014, *MNRAS*, **445**, 1084
- de Oliveira-Costa A., Tegmark M., Gaensler B. M., Jonas J., Landecker

T. L., Reich P., 2008, *MNRAS*, **388**, 247

de Vos M., Gunst A., Nijboer R., 2009, *Proceedings of the IEEE*, **97**, 1431

van Haarlem M. P., et al., 2013, *A&A*, **556**, A2

This paper has been typeset from a \LaTeX file prepared by the author.